Matter and
Radiation at Extremes

RESEARCH ARTICLE

scitation.org/journal/mre

Observation of a highly conductive warm dense state of water with ultrafast pump–probe free-electron-laser measurements

Cite as: Matter Radiat. Extremes 6, 054401 (2021); doi: 10.1063/5.0043726
Submitted: 11 January 2021 • Accepted: 23 June 2021 •
Published Online: 4 August 2021

Z. Chen,[1,a)] X. Na,[1] C. B. Curry,[1,2] S. Liang,[1] M. French,[3] A. Descamps,[1,4] D. P. DePonte,[1] J. D. Koralek,[1] J. B. Kim,[1] S. Lebovitz,[1,5] M. Nakatsutsumi,[6] B. K. Ofori-Okai,[1] R. Redmer,[3] C. Roedel,[7,8] M. Schörner,[3] S. Skruszewicz,[9] P. Sperling,[6] S. Toleikis,[9] M. Z. Mo,[1] and S. H. Glenzer[1,a)]

AFFILIATIONS

[1]SLAC National Accelerator Laboratory, Menlo Park, California 94025, USA
[2]University of Alberta, Edmonton, Alberta T6G 1H9, Canada
[3]Institute of Physics, University of Rostock, D-18051 Rostock, Germany
[4]Aeronautics and Astronautics Department, Stanford University, Stanford, California 94305, USA
[5]Northwestern University, Evanston, Illinois 60208, USA
[6]European XFEL, 22869 Schenefeld, Germany
[7]Friedrich Schiller University Jena, 07743 Jena, Germany
[8]Technical University Darmstadt, 64289 Darmstadt, Germany
[9]Deutsches Elektronen-Synchrotron DESY, 22607 Hamburg, Germany

Note: This paper is part of the Special Issue on Matter in Extreme States Created by Laser.

[a)]**Authors to whom correspondence should be addressed:** zchen@slac.stanford.edu and glenzer@slac.stanford.edu

ABSTRACT

The electrical conductivity of water under extreme temperatures and densities plays a central role in modeling planetary magnetic fields. Experimental data are vital to test theories of high-energy-density water and assess the possible development and presence of extraterrestrial life. These states are also important in biology and chemistry studies when specimens in water are confined and excited using ultrafast optical or free-electron lasers (FELs). Here we utilize femtosecond optical lasers to measure the transient reflection and transmission of ultrathin water sheet samples uniformly heated by a 13.6 nm FEL approaching a highly conducting state at electron temperatures exceeding 20 000 K. The experiment probes the trajectory of water through the high-energy-density phase space and provides insights into changes in the index of refraction, charge carrier densities, and AC electrical conductivity at optical frequencies. At excitation energy densities exceeding 10 MJ/kg, the index of refraction falls to $n = 0.7$, and the thermally excited free-carrier density reaches $n_e = 5 \times 10^{27}\ \mathrm{m}^{-3}$, which is over an order of magnitude higher than that of the electron carriers produced by direct photoionization. Significant specular reflection is observed owing to critical electron density shielding of electromagnetic waves. The measured optical conductivity reaches 2×10^4 S/m, a value that is one to two orders of magnitude lower than those of simple metals in a liquid state. At electron temperatures below 15 000 K, the experimental results agree well with the theoretical calculations using density-functional theory/molecular-dynamics simulations. With increasing temperature, the electron density increases and the system approaches a Fermi distribution. In this regime, the conductivities agree better with predictions from the Ziman theory of liquid metals.

© 2021 Author(s). All article content, except where otherwise noted, is licensed under a Creative Commons Attribution (CC BY) license (http://creativecommons.org/licenses/by/4.0/). https://doi.org/10.1063/5.0043726

I. INTRODUCTION

Water has been extensively studied because of its ubiquity and importance for a variety of fundamental processes and technologies. In its liquid phase, water exhibits many thermodynamic anomalies that originate from its well-connected hydrogen bond network.[1–3] Water not only plays a prominent role as a solvent in chemistry and biology,[4,5] but is also used as a reactant in energy research and technology.[6] Further, water is a key ingredient for many cosmic and planetary processes.[7] For instance, water and water–ice mixtures are highly abundant in ice giant planets such as Uranus or Neptune.[8–10] The high pressures and temperatures in the cores of these planets can create diamond from methane,[11] and the polymorphs of water under such conditions might become conductors capable of generating magnetic fields.[12,13]

Yet, our understanding of the fundamental properties of water remains limited. One key challenge is the accurate determination of its electrical conductivity in the so-called warm dense matter (WDM) regime that typically spans electron-volt temperatures at near-solid densities.[14–16] On the one hand, this is driven by its practical importance in understanding planetary processes such as the generation of the magnetic fields of Uranus and Neptune.[12,13,17] A representative example falling into this category is the recent measurement of the optical reflection of shock-compressed water.[18–20] Characteristic changes in reflectivity and electrical conductivity indicated the existence of superionic water ice under planetary interior conditions.[21]

On the other hand, water under extreme conditions[22] is also important for a vast number of x-ray free-electron-laser (XFEL) experiments in physics,[23] chemistry,[24] and biology,[25] where the interaction of short and intense XFEL pulses will lead to warm dense conditions. Further, the transport properties of warm dense water play a crucial role in evaluating sample environments and their effect on the dynamics under study. In particular, the electrical conductivity is determined by the mobile-electron density, the ionic structure, and the interaction between electrons and ions.[26] An intense XFEL can excite an enormous number of electrons, modifying the potential landscapes of the electrons and ions. While there has been some experimental effort to understand the structural properties of water using x-ray diffraction techniques,[27] measurements of its electrical conductivity under well-characterized WDM conditions are still lacking.

To determine the electrical conductivity of WDM generally requires measurements of the optical reflection and transmission of an excited sample.[28–30] The AC electrical conductivity at the frequency of an optical probe pulse is deduced accordingly. These measurements require the sample surface to be optically flat. The recent development of gas-dynamic liquid nozzles allows the delivery of these liquid samples with submicrometer thickness.[31] It opens a unique avenue to study the electrical conductivity of XFEL-excited WDM at high repetition rate. Here, we achieve a warm dense state of water by irradiating an ultrathin water sheet jet with $\lambda = 13.6$ nm radiation produced by an FEL at 10 Hz, reaching electron temperatures in the range of 10 000–20 000 K at the mass density of ambient liquid water.

The AC electrical conductivity was determined from simultaneous measurement of the optical reflection and transmission of ultrafast probe pulses at two different wavelengths, namely, 750 and 850 nm. Since the photon energies of these two probe wavelengths are below the bandgap between the highest occupied molecular orbital (HOMO) and the lowest unoccupied molecular orbital (LUMO) of water, as well as below the vertical binding energy of solvated electrons in water,[32] we expect the measured conductivity to be dominated by the contributions from the electrons in the conduction band of the excited water.

At the highest excitation energy densities, we observed that the index of refraction falls to $n = 0.7$, and the free-carrier density exceeds $n_e = 10^{27}$ m^{-3}, which is much higher than the density estimated by direct photoionization and is believed to be the result of carrier multiplication during thermalization of excited electrons. Further, the heated samples reach an optical conductivity of up to 2×10^4 S/m, within two orders of magnitude of the values in liquid phase simple metals.[33] In parallel, the samples become reflective and exhibit shielding of the laser light. At moderate temperatures, the experimental results agree well with theoretical calculations using density-functional theory coupled with molecular dynamics (DFT-MD).[13] At temperatures exceeding 15 000 K, the measurements agree better with the predictions from Ziman theory,[34] which is a manifestation of the liquid-metal-like electrical properties.

II. EXPERIMENT

The experiment was carried out in the BL3 end-station of the Free-Electron Laser in Hamburg (FLASH) facility at the Deutsches Elektronen-Synchrotron (DESY). We utilized 225 eV extreme ultraviolet (XUV) FEL pulses to excite and heat free-standing water sheet-jet samples to a maximum energy density of 12 MJ/kg. The specular reflection and transmission of the excited water were measured simultaneously as functions of the pump–probe delay time for two individual optical wavelengths to determine the complex reflective index and the optical conductivity of the excited water. Detailed descriptions of the experiment are given below.

A. Experimental setup and data acquisition

The free-standing ultrathin water samples were delivered by a microfluidic gas-dynamic nozzle; the details of the system are described elsewhere.[31] In brief, ultrapure liquid water (HPLC Plus grade, Sigma-Aldrich) was accelerated and flattened by pressurized helium gas, forming an optically flat water leaf 300 μm in height and 80 μm in width right below the nozzle exit. The thickness of the water leaf varied from ~1 μm at the nozzle exit position to less than 100 nm at the other end of the leaf. The sample thickness was determined as a function of position from thin-film interferometry on the reflection images. Instead of using a white light source to form color fringes,[31] the constructive and destructive fringes from the probe pulses were employed for *in situ* measurements. The interference pattern was calculated as a function of thickness according to the approach described in Ref. 35. Because the film thickness increased continuously from the bottom to the top of the water leaf,[31] we first identified the first constructive fringe from the bottom and used it as a reference point to determine the thickness at different positions based on the local reflectivity.

Figure 1 shows a schematic of the experimental setup. The FEL pulses excited the sample at normal incidence. The FEL pulse energies were measured by online gas-monitor detectors (GMDs) and varied in the range of 10–50 μJ during the measurements. The FEL pulse duration was shorter than 50 fs full width at half maximum (FWHM).[36] The FEL pulses were relayed into the sample chamber through grazing angle reflections from carbon and nickel-coated mirrors that had a combined efficiency of ~63%. These pulses were then focused onto the sample surface by an ellipsoidal mirror with a focal length $f = 2$ m and a reflectivity of 84% at 225 eV.[36] The focal spot was measured to have an elliptical profile with FWHM dimensions of 45 (vertical) $\times$ 24 μm^2 (horizontal). The FEL was operated at a repetition rate of 10 Hz, which provided sufficient time between shots for the water leaf to replenish itself. This ensured that

© Author(s) 2021

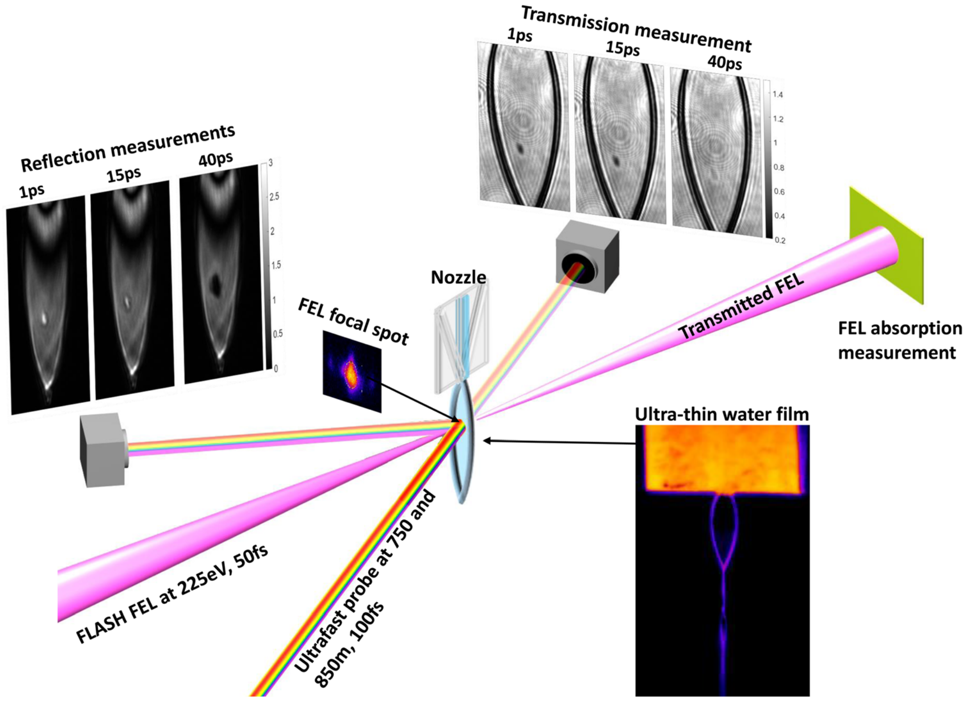

FIG. 1. Schematic of the experimental setup. An optically smooth water thin film was generated from a gas-dynamic liquid nozzle. The thin film was heated by the FLASH XUV-FEL focused by an ellipsoidal mirror to 45 × 24 μm^2 FWHM. The transmitted ratio of the FEL energy was measured by a YAG screen. The optical reflection and transmission of the thin film sample were probed by 750 and 850 nm, 100 fs FWHM laser pulses generated from an optical parametric amplifier. The measurement was carried out continuously at 10 Hz. Examples of reflection and transmission data measured by the 850 nm probe at an energy density of 9.1 ± 1.2 MJ/kg are shown.

each pump–probe measurement was carried out on a fresh water sample. The absorption of the FEL pulses was measured by an yttrium aluminum garnet (YAG) screen-based detector that was located 1 m after the sample. By monitoring the FEL-induced fluorescence intensity on a YAG screen with and without the water sample, we found that the XUV transmission ratios through 200 and 300 nm thick water were (82.2 ± 2.6) and (77.4 ± 2.7)%, respectively, which are in close agreement with the values of 83.1 and 75.9% predicted by the well-known XUV transmission model.[37] Because of these high transmission ratios, the FEL energy deposition can be considered to be uniform along the direction of propagation inside the sample. This allows us to calculate the absorbed energy density ΔE from the FEL fluence via the expression $\Delta E = \alpha F/d$, where α is the FEL absorption ratio, F is the incident FEL fluence, and d is the sample thickness.

Time-resolved reflectivity and transmissivity measurements of the excited water were obtained using 100 fs FWHM laser light at wavelengths of 750 and 850 nm. Probe pulses were generated from an optical parametric amplifier (OPA) that was driven by 800 nm, 60 fs pulses from a Ti:sapphire laser system. Owing to the nonlinear frequency conversion in the OPA system, the pre- and post-pulses of the fundamental laser pulses were improved. These probe beams were collimated by a 1 mm diameter iris that was 2 m upstream from the sample, so that the full water leaf could be uniformly illuminated and imaged. In both cases, the probe laser was S-polarized and then incident on the sample at an angle of 22.5°. The reflection and transmission images of the water leaf were recorded on two cameras. The time-resolved measurements were scanned from −2 to 50 ps after the excitation. The step size was 0.1 ps from −2 to 5 ps, after which it was increased to 1 ps, with 100 measurements collected at each time step.

B. Analysis of the probe beam reflection and transmission

For each probe wavelength, over 10 000 data shots were collected over the entire time scan. To compensate for the shot-to-shot fluctuations of the FEL, the energy of each FEL pulse recorded by a GMD was used to group the acquired data within a range of ±2.5 μJ (e.g., 10 ± 2.5 μJ). Between 1000 and 2000 independent measurements were analyzed in each pulse energy range. The reflection (R) and transmission (T) ratio values of the heated samples were derived from the recorded images. On each image, R and T were determined by comparing the relative brightness of the heated region with several reference regions. An example of data analysis is shown in Fig. 2.

In the reflection image [Fig. 2(a)], the curved thin-film interference pattern resulting from the gradient in jet thickness was flattened using a cross-correlation method as shown in the figure. The averaged pixel count in the FEL-heated region (6 × 6 pixel^2 in the region of interest) was normalized to the maximum and minimum intensities of the thin-film interference pattern. The absolute reflectivity was determined as

$$R = R_{\mathrm{peak}} \frac{I_R^{\mathrm{FEL}} - I_R^{\mathrm{min}}}{I_R^{\mathrm{max}} - I_R^{\mathrm{min}}}, \tag{1}$$

© Author(s) 2021

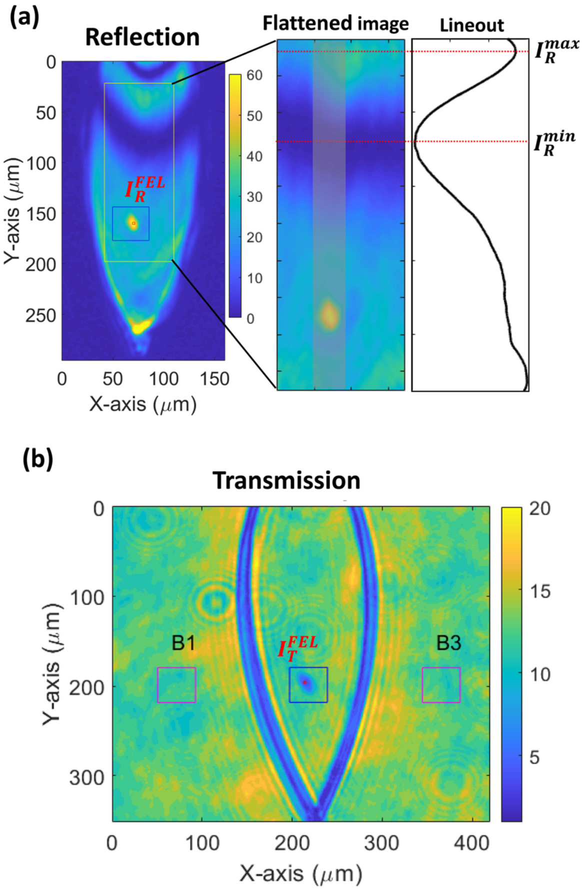

FIG. 2. Examples of the reflection and transmission data analysis. The data were acquired using the 850 nm probe at 300 fs after FEL excitation. (a) The raw reflection image on the left contains curved interference fringes, and the FEL-heated region is marked by the blue box. The average count at the center of the FEL-heated area (small red dot) is used as I_R^{FEL} in Eq. (1). The fringes inside the yellow box were flattened by a cross-correlation function, and the result is shown in the middle. The lineout taken from the flattened image is shown on the right, where I_R^{max} and I_R^{min} are obtained for use in Eq. (1). The gray band in the flattened image containing the FEL-heated region is excluded when we calculate the lineout curve. (b) The center of the FEL-heated region (small red dot) in the raw transmission image is used to determined I_T^{FEL} in Eq. (2). The vacuum areas in boxes B1 and B3 are used to determine the reference vacuum transmission I_T^{v} in the same equation. The distances from B1 and B3 to the FEL-heated spot are the same.

where $R_{\mathrm{peak}} = 0.0965$ is the peak reflectivity due to thin-film interference,[35] I_R^{FEL} is the average intensity in counts on the detector in the FEL-heated area, and I_R^{max} and I_R^{min} are the maximum and minimum intensities on the detector along the interference pattern. All these values were determined on the same image so that the shot-to-shot fluctuations of the probe pulse intensity were corrected.

In the transmission image [Fig. 2(b)], the pixel counts in the FEL-heated region are normalized to areas without sample, where 100% transmission is expected. The absolute transmission is obtained as

$$T = \frac{I_T^{\mathrm{FEL}}}{I_T^{v}} C_{\mathrm{Norm}}, \qquad (2)$$

where I_T^{FEL} and I_T^{v} are the average counts in the FEL-heated area and without the sample, respectively, and C_{Norm} is a normalization factor to compensate for the spatial heterogeneity of the probe and is determined from the data before FEL heating by the requirement that $R + T = 1$ when $t < -0.1$ ps. We set $I_T^{v} = (I_T^{B1} + I_T^{B3})/2$ to balance the vacuum transmission on both sides of the water sample.

The time-dependent reflection and transmission at different excitation energy densities measured by the 750 and 850 nm probe pulses are shown in Fig. 3. Immediately after the XUV-FEL heating, we observe a sharp increase in reflectivity and a rapid decrease in transmission. These two effects result from the generation of conduction electrons. Initially, water molecules are ionized by absorption of XUV photons. However, the inelastic mean free path of 200 eV electrons in water is about 1 nm.[38] Thus, the electrons collide with neighboring water molecules, transfer their energy, and promote the electrons into the conduction band. The high density of excited electrons screens the electric field of the probe pulse, causing an increase in reflection and a decrease in transmission. At the same time, the excess electrons absorb energy, some of which is lost through collisions consistent with Ohm's law,[26] resulting in $R + T < 1$. At higher excitation energy densities, we observe higher reflectivity and lower transmission, consistent with the increased creation of free carriers.

The substantial increase in reflectivity indicates that the free-electron density in the heated water is comparable to the critical densities of the probe pulse wavelengths, namely, 2×10^{27} and 1.5×10^{27} m^{-3} for 750 and 850 nm photons, respectively. At an excitation energy density of 10 MJ/kg, we calculate that the number density of electrons created by the absorption of 225 eV photons is only 2.8×10^{26} m^{-3}.

Shortly after the reflection reaches its peak values, we find that it quickly drops to nearly zero in a significantly shorter time than the corresponding transmission data (>50 ps). The latter indicates that the electron–ion equilibrium time is much slower than for XUV-FEL-heated hydrogen under similar temperature conditions (2–3 ps).[39,40] This is expected, because the water molecules are much heavier than hydrogen. Further, the fast disappearance of the reflection is likely due to the formation of gradients on the sample surfaces.[41,42] The smearing of the vacuum–water interface suppresses the reflection,[43] but the absorption of the probe pulse is not affected. In the following subsections, we focus only on early-time data (<5 ps) before the gradient effects become significant.

C. Refractive index and conductivity determined from the experimental data

The reflectivity and transmissivity of an isotropic thin film are dictated by its refractive index, the sample thickness, and the polarization, incident angle, and wavelength of the probe beam. To determine the refractive index for our experimental data, we first use the transfer-matrix method[29,35] to calculate the corresponding reflection and transmission in 200 and 300 nm thick films over a wide range of refractive indices. Subsequently, we find the refractive indices that produce the reflection and transmission that match best with our measurements. Examples of the measurements using 750 and 850 nm probes are shown in Figs. 4 and 5, respectively, where panels (c) and (d) of each figure show the real and imaginary parts of the reflective index (n and k) as functions of delay time that correspond to the

©Author(s) 2021

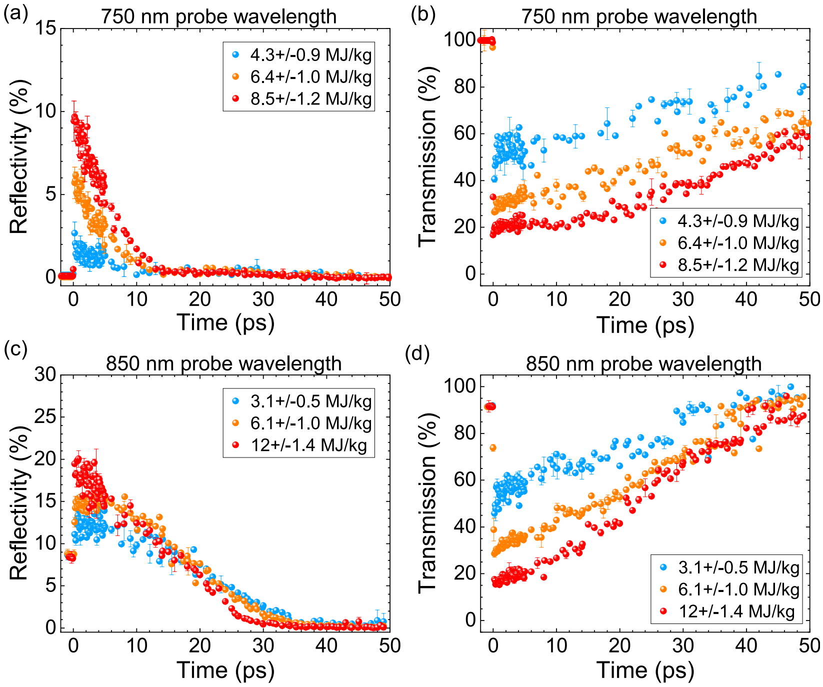

FIG. 3. Measured reflection and transmission data for a (300 ± 30) nm thin water film heated to various energy densities and measured by a 750 nm probe [(a) and (b)] and a (200 ± 20) nm thin film measured by a 850 nm probe [(c) and (d)]. The initial reflectivity in the 850 nm data is significantly higher than in the 750 nm data. This is because the 850 nm measurements were carried out near the peak intensity of the interference fringes, while the 750 nm measurements were near the minimum intensity of the fringes.

measured data in panels (a) and (b). The time step interval is 0.1 ps before 5 ps, and it increases to 1 ps at later time delay. About 10–20 individual data points were measured at each time step. The data points and the error bars represent the mean values and the standard deviations of the data measured at each time delay. In general, we find that n decreases from 1.33 to less than 1, a value that is characteristic of a plasma state. Simultaneously, k increases from zero to some fraction of unity. This high value of k indicates strong light absorption that is consistent with $R + T < 1$ after the FEL heating.

The real and imaginary parts of the inferred optical conductivity σ are shown in Figs. 4(e) and 4(f), respectively, for the 750 nm probe and in Figs. 5(e) and 5(f), respectively, for the 850 nm probe. The optical conductivity is a function of the complex refractive index and is given by[26]

$$\sigma = i[1 - (n + ik)^2]\epsilon_0\omega, \tag{3}$$

where ϵ_0 is the permittivity of free space and ω is the oscillation frequency of the probe beam. The square of the refractive index, i.e., $(n + ik)^2$, is equivalent to the complex dielectric function. The initial value of σ_r is 0, and $\sigma_i < 0$ at room temperature corresponds to typical dielectric material. We can see that upon FEL heating, both the real and imaginary parts increase to the order of 10^4 S/m. The trajectories of the measured reflection and transmission and the determined conductivity as functions of absorbed FEL energy density are shown in Figs. 6(a) and 6(b) for 750 nm probe pulses and in Figs. 6(c) and 6(d) for 850 nm probe pulses. Near the trajectories of the heated samples, the contour lines in reflection are nearly parallel to the vertical axis, indicating that the reflection is less sensitive to changes in σ_r than to changes in σ_i under our experimental conditions. On the other hand, the transmission data are sensitive to both σ_r and σ_i. The increase in σ_r indicates the rise in conduction electron density that enhances both the plasma shielding and reflection, but the higher σ_r also enhances the absorption of electromagnetic waves within the material[44] and attenuates the reflection. The competition between these effects therefore makes the reflection of the probe pulses less sensitive to σ_r.

III. THEORETICAL CALCULATIONS

To gain more insight into our experimental results, we used two different theoretical methods to calculate the electrical conductivity of the XUV-FEL-heated warm dense water. The first method was an implementation of the Kubo–Greenwood formalism based on density-functional theory coupled with molecular-dynamics simulations (DFT-MD).[45] The other method made use of the Ziman theory[34] of electrical conductivity based on an estimate of the electron density from DFT-MD and the total ionic structure factor computed from classical MD simulations.[46]

A. DFT-MD simulations

We performed DFT-MD simulations for water at the 1 g/cm^3 isochore with the Vienna *Ab initio* Simulation Package (VASP)[47–50] using 54 molecules and the Perdew–Burke–Ernzerhof (PBE) functional,[15,51] similar to what was done in earlier work.[13,52] To describe the ultrafast FEL experiment, we ran two-temperature simulations

© Author(s) 2021

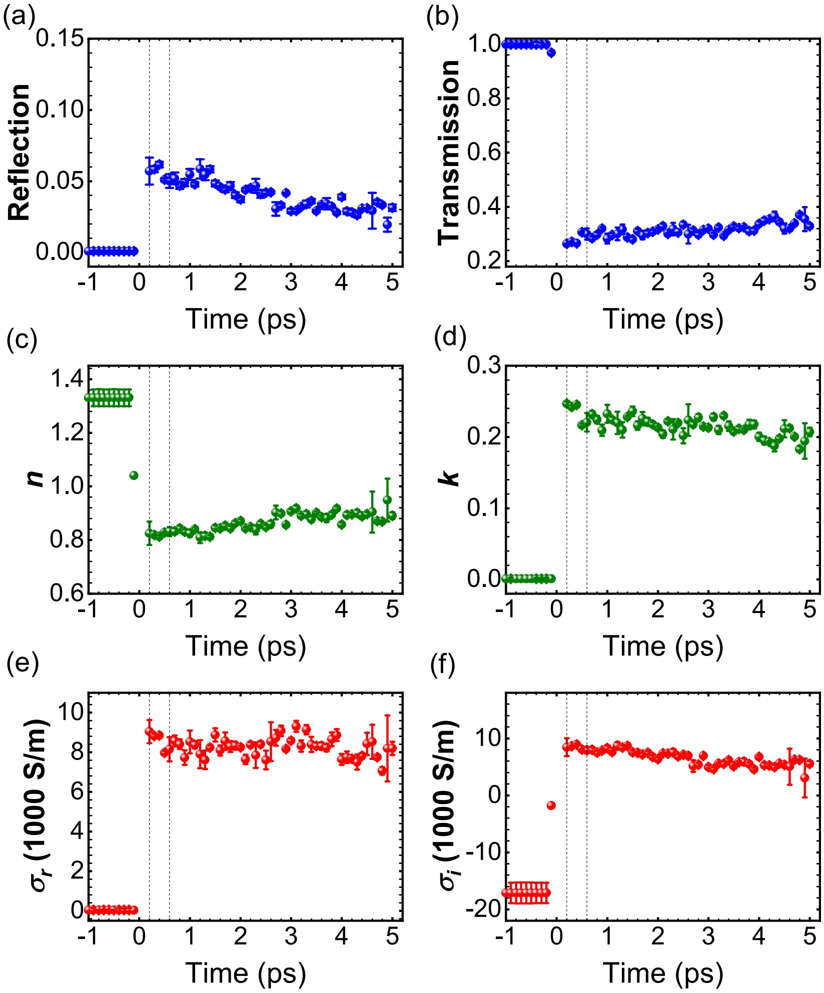

FIG. 4. Reflection and transmission measured using a probe wavelength of 750 nm, and the deduced complex refractive index and optical conductivity of water (300 nm thick) at an absorbed energy density of (6.1 ± 1) MJ/kg. (a) and (b) Averaged reflection and transmission at different time delays. (c) and (d) Complex refractive indices determined from Maxwell's equations implemented by the transform matrix method. (e) and (f) Real and imaginary parts of the corresponding electrical conductivity. The vertical dashed lines indicate the time window of 0.2–0.6 ps, where the electrical conductivity is obtained for further discussion.

with a constant ion temperature of $T_i = 300$ K and varied the electron temperature between 300 and 40 000 K. From the DFT-MD simulations, we obtained the isochoric heat capacity C_e of the electrons by numerical differentiation of the internal energy as shown in Fig. 7(a). The relation between the peak electron temperature T_e^{peak} and the absorbed FEL energy density ΔE is

$$\Delta E = \int_{300\,\mathrm{K}}^{T_e^{\mathrm{peak}}} C_e\,(T_e)\,dT_e. \tag{4}$$

It is worth noting that we assume all of the absorbed energy remains in the electron system within the first 0.5 ps after FEL heating. This assumption is supported by the long time scales of the measured reflection and transmission, which suggests that the electron–ion energy relaxation time scale is of the order of tens of picoseconds. Figure 7(b) shows the result for ΔE vs T_e.

The frequency-dependent conductivity $\sigma_r(\omega)$[45,53] was also calculated via the Kubo–Greenwood formalism[54,55] using the ionic configurations of all DFT-MD simulations and the Heyd–Scuseria–Ernzerhof (HSE) functional.[56] The imaginary parts of the conductivity at the probe laser wavelengths of 750 and 850 nm can also be determined using the Kramers–Kronig relations, analogously to the procedure described in Refs.[57,58], but it may be less accurate compared with the real part in the WDM regime.[29,59]

B. Ziman theory of conductivity in the framework of the Drude model

The real part of the optical conductivity is the sum of the free-carrier contribution and the contributions from interband transitions.[28] In the case of water, the photon energies of both 750 and 850 nm

© Author(s) 2021

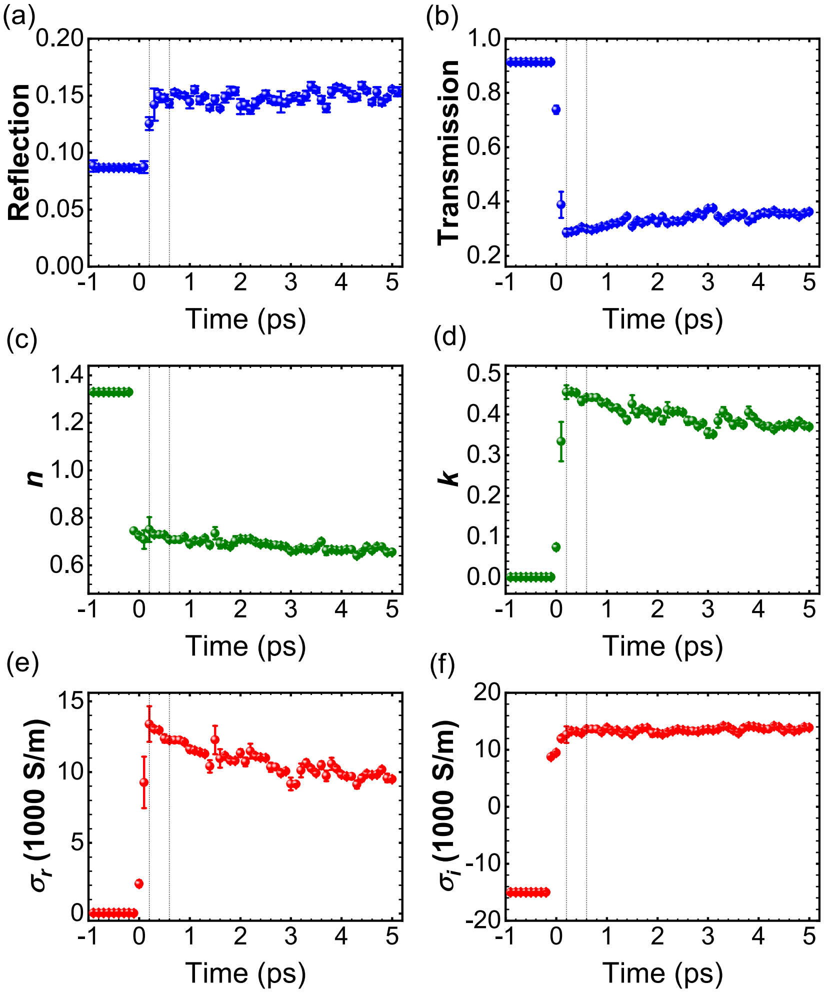

FIG. 5. Reflection and transmission measured using a probe wavelength of 850 nm, and the deduced complex refractive index and optical conductivity of water (200 nm thick) at an absorbed energy density of (6.1 ± 1) MJ/kg. (a) and (b) Averaged reflection and transmission at different time delays. (c) and (d) Complex refractive index determined from Maxwell's equations implemented by the transform matrix method. (e) and (f) Real and imaginary parts of the corresponding electrical conductivity. The vertical dashed lines indicate a time window of 0.2–0.6 ps, where the electrical conductivity is obtained for further discussion.

photons are below the interband transition energies and are insufficient to ionize conduction electrons to the continuum.[32] Thus, the Drude model can be employed to describe the free-carrier conductivity:[26]

$$\sigma_r = \frac{n_e e^2 \tau}{m_e[1 + (\omega\tau)^2]}, \tag{5}$$

where n_e is the carrier electron density, e is the unit charge, m_e is the electron rest mass, and τ is the electron relaxation time. The electron density as a function of temperature can be determined from the occupied electron density of states (DOS). We calculated the electron DOS using DFT-MD at various electron temperatures. Results for T_e at 300 and 20 000 K when $T_i = 300$ K are shown in Figs. 8(a) and 8(b), respectively. The values of n_e at different electron temperatures T_e can be determined by the integral of the Fermi distribution function $f_{T_e}(E)$ times the electron DOS $g_{T_e}(E)$:

$$n(T_e) = \int_{\mu}^{E_{\max}} f_{T_e}(E) g_{T_e}(E)\, dE, \tag{6}$$

where μ is the chemical potential, which is determined by conservation of the total number of valence and conduction electrons.[59] The T_e-dependent carrier density is shown in Fig. 9(a). At $T_e = 5000$ K, n_e is negligible. It starts to increase significantly at higher temperatures, reaching 5×10^{27} m^{-3} at T_e = 20 000 K, which corresponds to an absorbed energy density of 11.6 MJ/kg. This electron carrier density is equal to 2.5 times the critical density for 750 nm light, confirming that our observed increase in probe beam reflectivity is a result of a high density of conduction electrons. Figure 9(b) shows the electron degeneracy parameter Θ, which is the ratio of the thermal energy to the Fermi energy. Because n_e increases rapidly as a function of T_e, the excited electrons become more degenerate at higher temperatures.

© Author(s) 2021

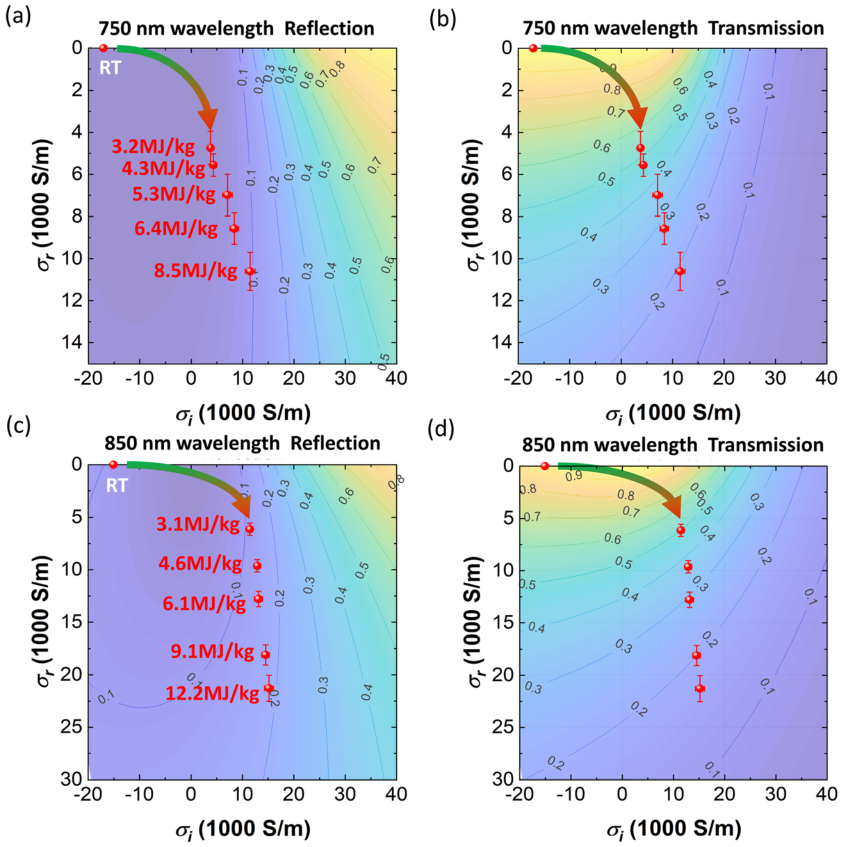

FIG. 6. Real and imaginary parts of the electrical conductivity from cold and heated water (0.2–0.6 ps after FEL heating, with the error bars representing the standard deviations of the data within this time interval) on the contour plots of reflection and transmission. (a) and (b) 750 nm laser probe on a 300 nm thick sample, with the heated-state samples being measured at energy densities of (3.2 ± 0.8), (4.3 ± 0.9), (5.3 ± 0.9), (6.4 ± 1), and (8.5 ± 1.2) MJ/kg, respectively. (c) and (d) 850 nm laser probe on a 200 nm thick sample, with the heated-state samples being measured at energy densities of (3.1 ± 0.8), (4.6 ± 0.9), (6.1 ± 1), (9.1 ± 1.2), and (12 ± 1.4) MJ/kg, respectively. The room temperature data (RT, i.e., $T_e = T_i = 300$ K) are shown at the top left corner in each plot.

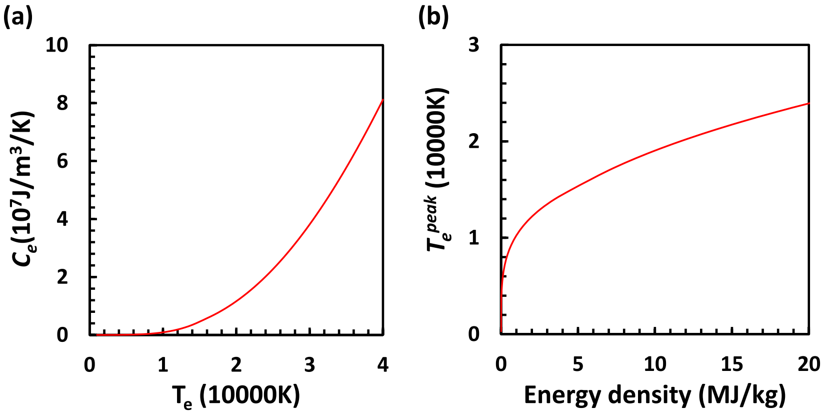

FIG. 7. (a) Electron specific heat capacity as a function of electron temperature from DFT calculations. (b) Peak electron temperature as a function of absorbed XUV energy density, calculated using Eq. (4).

© Author(s) 2021

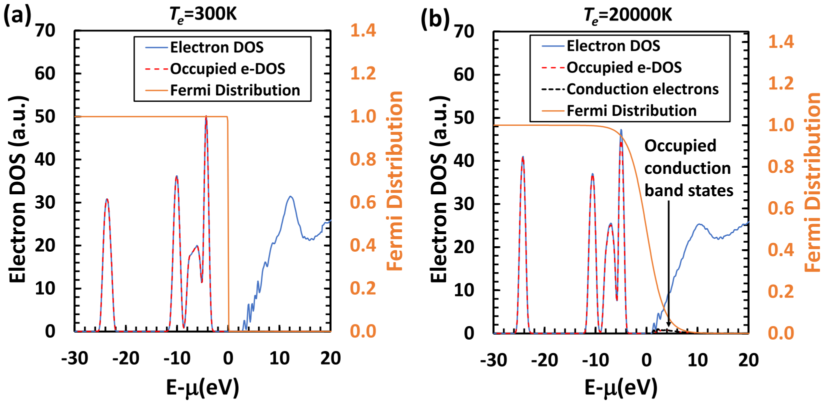

FIG. 8. Electron DOS (e-DOS) of water from DFT calculations at electron temperatures of (a) 300 K and (b) 20 000 K. The ion temperature is 300 K in both cases.

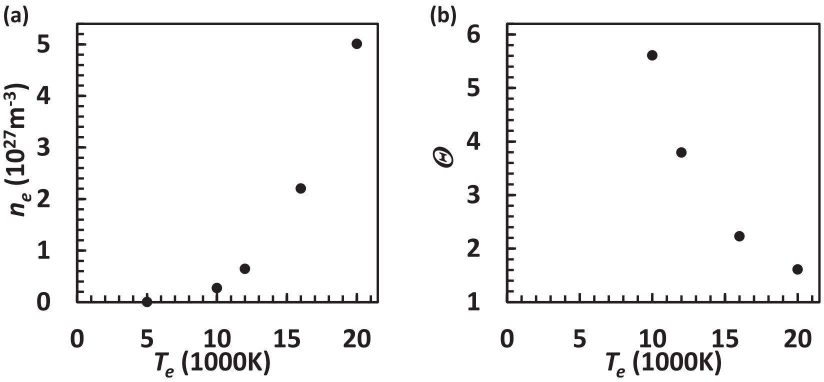

FIG. 9. (a) Density of conduction (carrier) electrons as a function of T_e calculated using the results for the electron DOS and Eq. (6). (b) The corresponding electron degeneracy parameter Θ.

The electron relaxation time τ is the inverse of the scattering frequency υ. We note that υ is very sensitive to changes in temperature and density. For our experimental conditions, the contribution from electron–electron scattering is small, because the conduction electron density is still low compared with the atomic density (10^{29} m^{-3}). Thus, υ is dominated by electron–ion scattering, i.e., $\upsilon \approx \upsilon_{ei}$. The Ziman theory of conductivity enables determination of υ_{ei} based on knowledge of the ionic structure factor S_{ii} according to[60]

$$\upsilon_{ei} = \frac{n_i m_e}{2p_F^3}\int_0^{2k_F}\left|\frac{4\pi e^2}{Q^2+k_e^2}\right|^2 Q^3 S_{ii}(Q)\frac{dQ}{2\pi}, \tag{7}$$

where Q is the momentum transfer vector, k_e is the electron screening vector, which is determined from the electron temperature and density,[61] n_i is the molecular density, m_e is the electron rest mass, and k_F and p_F are the Fermi wave vector and momentum of the free carriers, respectively.

To estimate the structure factor of liquid water, S_{ii}, classical MD simulations were performed at different temperatures under the condition of thermal equilibrium, i.e., $T_e = T_i$. Here, the use of classical MD allows us to model a much larger simulation box so that the lower-Q range of S_{ii} can be accessed, which is needed to compute υ_{ei} using Eq. (7). The simulation cell contained 1024 water molecules with density ρ = 0.999 g/cm^3 and was performed under the constant-temperature, constant-volume (NVT) ensemble using the TIP4P/2005 force field.[62] At each temperature, the system was equilibrated for 1 ns, and configurations were collected over the following 500 ps. The ion–ion structure factor was computed via

$$S_{ii}(Q) = \frac{1}{N}\left\langle \sum_{p=1}^{N}\sum_{q=1}^{N} e^{-iQr_{pq}}\right\rangle, \tag{8}$$

where Q is truncated at $2\pi/d \approx 0.2$ Å^{-1} with a box size of d = 31.3 Å, and r_{pq} is the distance between ions p and q.

The S_{ii} results for four different temperatures are shown in Fig. 10. Our result at room temperature is verified with data reported for the O–O structure factor measured by X-ray scattering.[63] The average difference at each Q is calculated to be within 4.6%. As the temperature increases, we see that the primary liquid peak moves toward higher Q, while its peak height does not seem to change significantly. According to MD simulations, the increase in temperature stretches the correlation peaks in real space, which results in a contraction of the first atomic peak in the total

© Author(s) 2021

radial distribution function. This is manifested by the primary liquid peak shifting to high Q, as observed in Fig. 10.

IV. COMPARISON OF EXPERIMENTAL DATA WITH THEORETICAL CALCULATIONS

Figure 11 shows a comparison of the experimental data at 750 and 850 nm with theoretical calculations from DFT-MD and the Ziman theory. The experimental data at time delays between 0.2 and 0.6 ps are averaged. At these time delays, most of the absorbed FEL energy should be in the electron system, while the molecules remain cold. Accordingly, both calculations are carried out using the peak electron temperatures at the corresponding energy densities [see Fig. 9(a)] and the ion temperature at 300 K. The σ_r measured at both 750 and 850 nm increases as a function of T_e. The 850 nm conductivity is higher than that at 750 nm. This is a typical Drude-like behavior according to Eq. (5), i.e., σ_r decreases as the frequency of the electric field ω increases. We observe a similar trend in the theoretical calculations. The DFT-MD calculations agree well with the measurements up to $T_e = 15\,000$ K, especially with the 850 nm data. At higher temperatures, the DFT-MD calculations overestimate σ_r. By contrast, the Ziman theory calculations underestimate the results at $T_e < 15\,000$ K, but start to show better agreement at higher temperatures.

The failure of the Ziman theory at low temperatures is likely due to the low electron degeneracy under these conditions, i.e., $\Theta \gg 1$, as shown in Fig. 9(b). In this regime, there is no well-defined Fermi surface of the electrons. As the electron temperature increases, the conduction band is populated, and Θ approaches unity near $T_e = 20\,000$ K. Consequently, the heated water behaves more like a liquid metal, and its conductivity can be better described by the Ziman theory. Note that as T_i increases, the S_{ii} data below $Q = 2k_F$ also increase, as shown in Fig. 10. This will raise υ_{ei}, as indicated in Eq. (7). At the same time, the conduction band electron density will decrease as energy couples to the ions. These two effects together in turn reduce the magnitude of σ_r, resulting in less agreement with the experimental data, i.e., σ_r will drop by ~20 and ~45% if we assume $T_i = 500$ and 1000 K, respectively, in the Ziman theory calculations. The DFT-MD calculations properly describe the weakly degenerate conditions at low temperatures. However, at this point, it is not clear why they do not work at higher temperatures. It is possible that the exchange and correlation functional used in the DFT cannot correctly model the chemical processes under the strongly excited conditions attained in our experiment. Therefore, our measurements provide valuable data to test these theoretical calculations, especially in nonequilibrium states produced by ultrafast laser or FEL excitation, where the electron temperature is significantly higher than the ion temperature.[29]

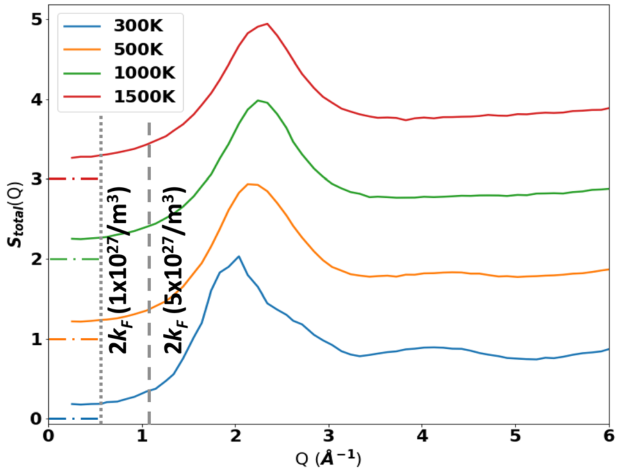

FIG. 10. Total structure factor of water calculated by MD simulations at equilibrium temperatures ($T_e = T_i$) of 300, 500, 1000, and 1500 K. The baseline of each curve is shown by the dash-dotted lines on the left using the corresponding colors. The vertical dotted line and dashed line correspond to twice the Fermi vector, i.e., the upper bound of the integral in Eq. (7) at carrier densities of 1×10^{27} and 5×10^{27} m^{-3}, respectively.

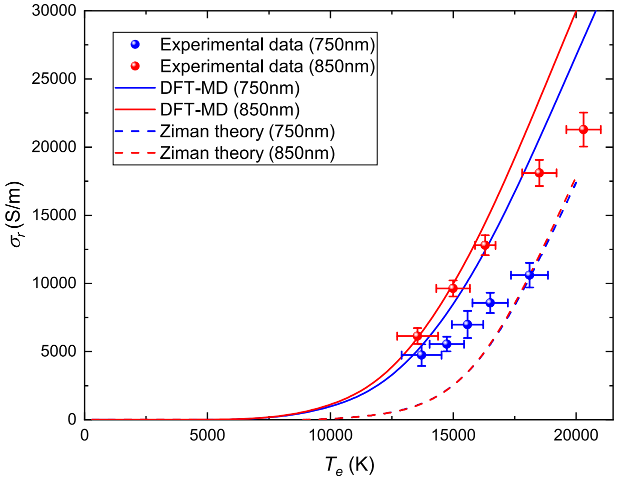

FIG. 11. Optical conductivity as a function of electron temperature T_e: a comparison of experiments and theoretical calculations. Both DFT-MD and Ziman theory calculations were performed at $T_i = 300$ K. The vertical error bars are inherited from Fig. 6, and the horizontal error bars correspond to the range of energy densities in the data.

V. CONCLUSIONS

Using XUV-FEL pulses to excite optically flat ultrathin water samples, we have demonstrated the first optical conductivity measurements of isochorically heated warm dense water at a continuous 10 Hz repetition rate. We have acquired the conductivity data at the first 0.5 ps following the FEL excitation, when electron temperatures reach up to 20 000 K while the ions remain cold. The results have allowed us to test nonequilibrium calculations using DFT-MD and the Ziman theory. We have found that although the DFT-MD calculations can describe the conductivity results at electron temperatures below 15 000 K, further effort is needed to improve their accuracy to predict the conductivity at higher temperatures. Instead, agreement with the Ziman theory calculations is found when T_e approaches 20 000 K, which indicates that the strongly excited water exhibits liquid-metal-like behavior when a large number of electrons are excited to the conduction band. Our results bring new insight into a WDM regime that is relevant for both high-energy-density physics and ultrafast studies in chemistry and biology. In the future investigations, we plan to acquire conductivity data with longer time

© Author(s) 2021

delays so that the samples approach equilibrium conditions. These data could be obtained by transmission ellipsometry or interferometry measurements.

ACKNOWLEDGMENTS

This work was supported by the U.S. Department of Energy, Office of Science, Fusion Energy Science under Grant No. FWP 100182. C.B.C. acknowledges partial support from the Natural Sciences and Engineering Research Council of Canada (NSERC). J.D.K. and D.P.D. are supported by the U.S. Department of Energy, Office of Science, Office of Basic Energy Sciences under Contract No. DE-AC02-76SF00515. M.Z.M. acknowledges partial support from the U.S. Department of Energy, Laboratory Directed Research and Development (LDRD) Program at SLAC National Accelerator Laboratory, under Contract No. DE-AC02-76SF00515. M.F. and R.R. thank the Deutsche Forschungsemeinschaft (DFG) for support within the Research Unit Grant No. FOR 2440. The DFT-MD calculations were performed at the North-German Supercomputing Alliance (HLRN) facilities. The work of S.L. was supported in part by the U.S. Department of Energy, Office of Science, Office of Workforce Development for Teachers and Scientists (WDTS) under the Science Undergraduate Laboratory Internships (SULI) Program. C.R. acknowledges support from the LOEWE Excellence Initiative of the State of Hessen.

REFERENCES

[1] J. A. Sellberg, C. Huang, T. A. McQueen, N. D. Loh, H. Laksmono, D. Schlesinger, R. G. Sierra, D. Nordlund, C. Y. Hampton, D. Starodub, D. P. DePonte, M. Beye, C. Chen, A. V. Martin, A. Barty, K. T. Wikfeldt, T. M. Weiss, C. Caronna, J. Feldkamp, L. B. Skinner, M. M. Seibert, M. Messerschmidt, G. J. Williams, S. Boutet, L. G. M. Pettersson, M. J. Bogan, and A. Nilsson, "Ultrafast X-ray probing of water structure below the homogeneous ice nucleation temperature," Nature **510**, 381 (2014).

[2] K. H. Kim, A. Späh, H. Pathak, F. Perakis, D. Mariedahl, K. Amann-Winkel, J. A. Sellberg, J. H. Lee, S. Kim, J. Park, K. H. Nam, T. Katayama, and A. Nilsson, "Maxima in the thermodynamic response and correlation functions of deeply supercooled water," Science **358**, 1589 (2017).

[3] K. H. Kim, K. Amann-Winkel, N. Giovambattista, A. Späh, F. Perakis, H. Pathak, M. L. Parada, C. Yang, D. Mariedahl, T. Eklund, T. J. Lane, S. You, S. Jeong, M. Weston, J. H. Lee, I. Eom, M. Kim, J. Park, S. H. Chun, P. H. Poole, and A. Nilsson, "Experimental observation of the liquid-liquid transition in bulk supercooled water under pressure," Science **370**, 978 (2020).

[4] F. Perakis, L. De Marco, A. Shalit, F. Tang, Z. R. Kann, T. D. Kühne, R. Torre, M. Bonn, and Y. Nagata, "Vibrational spectroscopy and dynamics of water," Chem. Rev. **116**, 7590–7607 (2016).

[5] H.-X. Zhou and X. Pang, "Electrostatic interactions in protein structure, folding, binding, and condensation," Chem. Rev. **118**, 1691–1741 (2018).

[6] V. Maurice and P. Marcus, "Progress in corrosion science at atomic and nanometric scales," Prog. Mater. Sci. **95**, 132–171 (2018).

[7] W. B. Hubbard, "Interiors of the giant planets," Science **214**, 145–149 (1981).

[8] R. Redmer, T. R. Mattsson, N. Nettelmann, and M. French, "The phase diagram of water and the magnetic fields of Uranus and Neptune," Icarus **211**, 798 (2011).

[9] S. Stanley and J. Bloxham, "Convective-region geometry as the cause of Uranus' and Neptune's unusual magnetic fields," Nature **428**, 151 (2004).

[10] S. Stanley and J. Bloxham, "Numerical dynamo models of Uranus' and Neptune's magnetic fields," Icarus **184**, 556 (2006).

[11] D. Kraus, J. Vorberger, A. Pak, N. J. Hartley, L. B. Fletcher, S. Frydrych, E. Galtier, E. J. Gamboa, D. O. Gericke, S. H. Glenzer, E. Granados, M. J. MacDonald, A. J. MacKinnon, E. E. McBride, I. Nam, P. Neumayer, M. Roth, A. M. Saunders, A. K. Schuster, P. Sun, T. van Driel, T. Döppner, and R. W. Falcone, "Formation of diamonds in laser-compressed hydrocarbons at planetary interior conditions," Nat. Astron. **1**, 606 (2017).

[12] N. F. Ness, M. H. Acuña, K. W. Behannon, L. F. Burlaga, J. E. P. Connerney, R. P. Lepping, and F. M. Neubauer, "Magnetic fields at Uranus," Science **233**, 85–89 (1986).

[13] M. French, T. R. Mattsson, N. Nettelmann, and R. Redmer, "Equation of state and phase diagram of water at ultrahigh pressures as in planetary interiors," Phys. Rev. B **79**, 054107 (2009).

[14] P. Sperling, E. J. Gamboa, H. J. Lee, H. K. Chung, E. Galtier, Y. Omarbakiyeva, H. Reinholz, G. Röpke, U. Zastrau, J. Hastings, L. B. Fletcher, and S. H. Glenzer, "Free-electron x-ray laser measurements of collisional-damped plasmons in isochorically heated warm dense matter," Phys. Rev. Lett. **115**, 115001 (2015).

[15] B. B. L. Witte, L. B. Fletcher, E. Galtier, E. Gamboa, H. J. Lee, U. Zastrau, R. Redmer, S. H. Glenzer, and P. Sperling, "Warm dense matter demonstrating non-drude conductivity from observations of nonlinear plasmon damping," Phys. Rev. Lett. **118**, 225001 (2017).

[16] B. B. L. Witte, G. Röpke, P. Neumayer, M. French, P. Sperling, V. Recoules, S. H. Glenzer, and R. Redmer, "Comment on "Isochoric, isobaric, and ultrafast conductivities of aluminum, lithium, and carbon in the warm dense matter regime"," Phys. Rev. E **99**, 047201 (2019).

[17] S. Frydrych, J. Vorberger, N. J. Hartley, A. K. Schuster, K. Ramakrishna, A. M. Saunders, T. van Driel, R. W. Falcone, L. B. Fletcher, E. Galtier, E. J. Gamboa, S. H. Glenzer, E. Granados, M. J. MacDonald, A. J. MacKinnon, E. E. McBride, I. Nam, P. Neumayer, A. Pak, K. Voigt, M. Roth, P. Sun, D. O. Gericke, T. Döppner, and D. Kraus, "Demonstration of X-ray Thomson scattering as diagnostics for miscibility in warm dense matter," Nat. Commun. **11**, 2620 (2020).

[18] P. M. Celliers, G. W. Collins, D. G. Hicks, M. Koenig, E. Henry, A. Benuzzi-Mounaix, D. Batani, D. K. Bradley, L. B. Da Silva, R. J. Wallace, S. J. Moon, J. H. Eggert, K. K. M. Lee, L. R. Benedetti, R. Jeanloz, I. Masclet, N. Dague, B. Marchet, M. Rabec Le Gloahec, C. Reverdin, J. Pasley, O. Willi, D. Neely, and C. Danson, "Electronic conduction in shock-compressed water," Phys. Plasmas **11**, L41 (2004).

[19] M. D. Knudson, M. P. Desjarlais, R. W. Lemke, T. R. Mattsson, M. French, N. Nettelmann, and R. Redmer, "Probing the interiors of the ice giants: Shock compression of water to 700 GPa and 3.8 g/cm^3," Phys. Rev. Lett. **108**, 091102 (2012).

[20] T. Kimura, N. Ozaki, T. Sano, T. Okuchi, T. Sano, K. Shimizu, K. Miyanishi, T. Terai, T. Kakeshita, Y. Sakawa, and R. Kodama, "P-ρ-T measurements of H_2O up to 260 GPa under laser-driven shock loading," J. Chem. Phys. **142**, 164504 (2015).

[21] M. Millot, S. Hamel, J. R. Rygg, P. M. Celliers, G. W. Collins, F. Coppari, D. E. Fratanduono, R. Jeanloz, D. C. Swift, and J. H. Eggert, "Experimental evidence for superionic water ice using shock compression," Nat. Phys. **14**, 297 (2018).

[22] C. A. Stan, D. Milathianaki, H. Laksmono, R. G. Sierra, T. A. McQueen, M. Messerschmidt, G. J. Williams, J. E. Koglin, T. J. Lane, M. J. Hayes, S. A. H. Guillet, M. Liang, A. L. Aquila, P. R. Willmott, J. S. Robinson, K. L. Gumerlock, S. Botha, K. Nass, I. Schlichting, R. L. Shoeman, H. A. Stone, and S. Boutet, "Liquid explosions induced by X-ray laser pulses," Nat. Phys. **12**, 966 (2016).

[23] S. H. Glenzer, L. B. Fletcher, E. Galtier, B. Nagler, R. Alonso-Mori, B. Barbrel, S. B. Brown, D. A. Chapman, Z. Chen, C. B. Curry, F. Fiuza, E. Gamboa, M. Gauthier, D. O. Gericke, A. Gleason, S. Goede, E. Granados, P. Heimann, J. Kim, D. Kraus, M. J. MacDonald, A. J. MacKinnon, R. Mishra, A. Ravasio, C. Roedel, P. Sperling, W. Schumaker, Y. Y. Tsui, J. Vorberger, U. Zastrau, A. Fry, W. E. White, J. B. Hasting, and H. J. Lee, "Matter under extreme conditions experiments at the Linac Coherent Light Source," J. Phys. B: At., Mol. Opt. Phys. **49**, 092001 (2016).

[24] J. Yang, J. P. F. Nunes, K. Ledbetter, E. Biasin, M. Centurion, Z. Chen, A. A. Cordones, C. Crissman, D. P. Deponte, S. H. Glenzer, M.-F. Lin, M. Mo, C. D. Rankine, X. Shen, T. J. A. Wolf, and X. Wang, "Structure retrieval in liquid-phase electron scattering," Phys. Chem. Chem. Phys **23**, 1308 (2020).

[25] T. Gorkhover, A. Ulmer, K. Ferguson, M. Bucher, F. R. N. C. Maia, J. Bielecki, T. Ekeberg, M. F. Hantke, B. J. Daurer, C. Nettelblad, J. Andreasson, A. Barty, P. Bruza, S. Carron, D. Hasse, J. Krzywinski, D. S. D. Larsson, A. Morgan, K. Mühlig, M. Müller, K. Okamoto, A. Pietrini, D. Rupp, M. Sauppe, G. Van Der Schot, M. Seibert, J. A. Sellberg, M. Svenda, M. Swiggers, N. Timneanu, D. Westphal, G. Williams, A. Zani, H. N. Chapman, G. Faigel, T. Möller, J. Hajdu, and C. Bostedt, "Femtosecond X-ray Fourier holography imaging of free-flying nanoparticles," Nat. Photonics **12**, 150 (2018).

© Author(s) 2021

[26]N. W. Ashcroft and N. D. Mermin, *Solid State Physics* (Harcourt Brace Jovanovich Publishers, Toronto, 1976).

[27]K. R. Beyerlein, H. O. Jönsson, R. Alonso-Mori, A. Aquila, S. Bajt, A. Barty, R. Bean, J. E. Koglin, M. Messerschmidt, D. Ragazzon, D. Sokaras, G. J. Williams, S. Hau-Riege, S. Boutet, H. N. Chapman, N. Tîmneanu, and C. Caleman, "Ultrafast nonthermal heating of water initiated by an X-ray free-electron laser," Proc. Natl. Acad. Sci. U. S. A. **115**, 5652 (2018).

[28]A. Ng, P. Sterne, S. Hansen, V. Recoules, Z. Chen, Y. Y. Tsui, and B. Wilson, "dc conductivity of two-temperature warm dense gold," Phys. Rev. E **94**, 033213 (2016).

[29]Z. Chen, B. Holst, S. E. Kirkwood, V. Sametoglu, M. Reid, Y. Y. Tsui, V. Recoules, and A. Ng, "Evolution of ac conductivity in nonequilibrium warm dense gold," Phys. Rev. Lett. **110**, 135001 (2013).

[30]K. Widmann, T. Ao, M. E. Foord, D. F. Price, A. D. Ellis, P. T. Springer, and A. Ng, "Single-state measurement of electrical conductivity of warm dense gold," Phys. Rev. Lett. **92**, 125002 (2004).

[31]J. D. Koralek, J. B. Kim, P. Brůža, C. B. Curry, Z. Chen, H. A. Bechtel, A. A. Cordones, P. Sperling, S. Toleikis, J. F. Kern, S. P. Moeller, S. H. Glenzer, and D. P. DePonte, "Generation and characterization of ultrathin free-flowing liquid sheets," Nat. Commun. **9**, 1353 (2018).

[32]V. Svoboda, R. Michiels, A. C. LaForge, J. Med, F. Stienkemeier, P. Slavíček, and H. J. Wörner, "Real-time observation of water radiolysis and hydrated electron formation induced by extreme-ultraviolet pulses," Sci. Adv. **6**, eaaz0385 (2020).

[33]R. A. Matula, "Electrical resistivity of copper, gold, palladium, and silver," J. Phys. Chem. Ref. Data **8**, 1147 (1979).

[34]J. M. Ziman, "A theory of the electrical properties of liquid metals. I: The monovalent metals," Philos. Mag. **6**, 1013 (1961).

[35]M. Born and E. Wolf, *Principles of Optics*, 6th ed. (Pergamon Press, Oxford, 1980).

[36]K. Tiedtke, A. Azima, N. von Bargen, L. Bittner, S. Bonfigt, S. Düsterer, B. Faatz, U. Frühling, M. Gensch, and Ch. Gerth, "The soft x-ray free-electron laser FLASH at DESY: Beamlines, diagnostics and end-stations," New J. Phys. **11**, 023029 (2009).

[37]B. L. Henke, E. M. Gullikson, and J. C. Davis, "X-ray interactions: Photoabsorption, scattering, transmission, and reflection at $E = 50$-30,000 eV, $Z = 1$-92," At. Data Nucl. Data Tables **54**, 181 (1993).

[38]R. Garcia-Molina, I. Abril, I. Kyriakou, and D. Emfietzoglou, "Inelastic scattering and energy loss of swift electron beams in biologically relevant materials," Surf. Interface Anal. **49**, 11 (2017).

[39]U. Zastrau, P. Sperling, A. Becker, T. Bornath, R. Bredow, T. Döppner, S. Dziarzhytski, T. Fennel, L. B. Fletcher, E. Förster, C. Fortmann, S. H. Glenzer, S. Göde, G. Gregori, M. Harmand, V. Hilbert, B. Holst, T. Laarmann, H. J. Lee, T. Ma, J. P. Mithen, R. Mitzner, C. D. Murphy, M. Nakatsutsumi, P. Neumayer, A. Przystawik, S. Roling, M. Schulz, B. Siemer, S. Skruszewicz, J. Tiggesbäumker, S. Toleikis, T. Tschentscher, T. White, M. Wöstmann, H. Zacharias, and R. Redmer, "Equilibration dynamics and conductivity of warm dense hydrogen," Phys. Rev. E **90**, 013104 (2014).

[40]U. Zastrau, P. Sperling, M. Harmand, A. Becker, T. Bornath, R. Bredow, S. Dziarzhytski, T. Fennel, L. B. Fletcher, E. Förster, S. Göde, G. Gregori, V. Hilbert, D. Hochhaus, B. Holst, T. Laarmann, H. J. Lee, T. Ma, J. P. Mithen, R. Mitzner, C. D. Murphy, M. Nakatsutsumi, P. Neumayer, A. Przystawik, S. Roling, M. Schulz, B. Siemer, S. Skruszewicz, J. Tiggesbäumker, S. Toleikis, T. Tschentscher, T. White, M. Wöstmann, H. Zacharias, T. Döppner, S. H. Glenzer, and R. Redmer, "Resolving ultrafast heating of dense cryogenic hydrogen," Phys. Rev. Lett. **112**, 105002 (2014).

[41]U. Samir, K. H. Wright, and N. H. Stone, "The expansion of a plasma into a vacuum: Basic phenomena and processes and applications to space plasma physics," Rev. Geophys. **21**, 1631 (1983).

[42]Z. Chen, M. Mo, L. Soulard, V. Recoules, P. Hering, Y. Y. Tsui, S. H. Glenzer, and A. Ng, "Interatomic potential in the nonequilibrium warm dense matter regime," Phys. Rev. Lett. **121**, 075002 (2018).

[43]W. H. Southwell, "Gradient-index antireflection coatings," Opt. Lett. **8**, 584 (1984).

[44]D. Fisher, M. Fraenkel, Z. Henis, E. Moshe, and S. Eliezer, "Interband and intraband (drude) contributions to femtosecond laser absorption in aluminum," Phys. Rev. E **65**, 016409 (2001).

[45]M. French and R. Redmer, "Electronic transport in partially ionized water plasmas," Phys. Plasmas **24**, 092306 (2017).

[46]R. Scipioni, L. Stixrude, and M. P. Desjarlais, "Electrical conductivity of SiO_2 at extreme conditions and planetary dynamos," Proc. Natl. Acad. Sci. U. S. A. **114**, 9009 (2017).

[47]G. Kresse and J. Hafner, "*Ab initio* molecular dynamics for liquid metals," Phys. Rev. B **47**, 558(R) (1993).

[48]G. Kresse and J. Hafner, "*Ab initio* molecular dynamics for open-shell transition metals," Phys. Rev. B **48**, 13115–13118 (1993).

[49]G. Kresse and J. Hafner, "*Ab initio* molecular-dynamics simulation of the liquid-metal–amorphous-semiconductor transition in germanium," Phys. Rev. B **49**, 14251–14269 (1994).

[50]G. Kresse and J. Furthmüller, "Efficient iterative schemes for *ab initio* total-energy calculations using a plane-wave basis set," Phys. Rev. B **54**, 11169–11186 (1996).

[51]J. P. Perdew, K. Burke, and M. Ernzerhof, "Generalized gradient approximation made simple," Phys. Rev. Lett. **77**, 3865–3868 (1996).

[52]M. French, T. R. Mattsson, and R. Redmer, "Diffusion and electrical conductivity in water at ultrahigh pressures," Phys. Rev. B **82**, 174108 (2010).

[53]M. Gajdoš, K. Hummer, G. Kresse, J. Furthmüller, and F. Bechstedt, "Linear optical properties in the projector-augmented wave methodology," Phys. Rev. B **73**, 045112 (2006).

[54]R. Kubo, "Statistical-mechanical theory of irreversible processes. I. General theory and simple applications to magnetic and conduction problems," J. Phys. Soc. Jpn. **12**, 570 (1957).

[55]D. A. Greenwood, "The Boltzmann equation in the theory of electrical conduction in metals," Proc. Phys. Soc. **71**, 585–596 (1958).

[56]J. Heyd, G. E. Scuseria, and M. Ernzerhof, "Erratum: "Hybrid functionals based on a screened Coulomb potential" [J. Chem. Phys. **118**, 8207 (2003)]," J. Chem. Phys. **124**, 219906 (2006).

[57]M. French and R. Redmer, "Optical properties of water at high temperature," Phys. Plasmas **18**, 043301 (2011).

[58]A. Ravasio, M. Bethkenhagen, J.-A. Hernandez, A. Benuzzi-Mounaix, F. Datchi, M. French, M. Guarguaglini, F. Lefevre, S. Ninet, R. Redmer, and T. Vinci, "Metallization of shock-compressed liquid ammonia," Phys. Rev. Lett. **126**, 025003 (2020).

[59]B. Holst, V. Recoules, S. Mazevet, M. Torrent, A. Ng, S. Kirkwood, V. Sametoglu, M. Reid, and Y. Y. Tsui, "*Ab initio* model on optical properties of non-equilibrium warm dense matter," Phys. Rev. B **90**, 035121 (2014).

[60]D. Kremp, M. Schlanges, and W.-D. Kraeft, *Quantum Statistics of Nonideal Plasmas* (Springer, Berlin, Heidelberg, 2005).

[61]S. H. Glenzer and R. Redmer, "X-ray Thomson scattering in high energy density plasmas," Rev. Mod. Phys. **81**, 1625 (2009).

[62]J. L. F. Abascal and C. Vega, "A general purpose model for the condensed phases of water: TIP4P/2005," J. Chem. Phys. **123**, 234505 (2005).

[63]G. Hura, J. M. Sorenson, R. M. Glaeser, and T. Head-Gordon, "High-quality x-ray scattering experiment on liquid water at ambient conditions," J. Chem. Phys. **113**, 9140 (2000).

© Author(s) 2021